MOX-Report No. 48/2024

# Addressing Atmospheric Absorption in Adaptive Rectangular Decomposition

Cicalese, G.; Ciaramella, G.; Mazzieri, I.

# Addressing Atmospheric Absorption in Adaptive Rectangular Decomposition

Gerardo Cicalese*, Gabriele Ciaramella, and Ilario Mazzieri

MOX - Laboratory for Modeling and Scientific Computing, Dipartimento di
Matematica, Politecnico di Milano, Piazza Leonardo da Vinci 32, Milan, 20133, Italy

July 4, 2024

## Abstract

This paper focuses on the Adaptive Rectangular Decomposition (ARD) scheme, a wave-based method utilized for acoustic simulations. ARD holds promise for diverse applications. In architectural design, it can forecast acoustical parameters, facilitating the creation of spaces with superior sound quality. Moreover, in the domain of Acoustic Virtual Reality, ARD can offer users a more immersive and lifelike acoustic environment. Our enhancement proves advantageous for all these applications, enabling the simulation of larger environments with heightened precision. Despite its notable efficiency, ARD faces a significant drawback: the absence of atmospheric absorption modeling. The principal aim of this study is to rectify this limitation, thereby augmenting the capabilities of the ARD algorithm.

---

*Corresponding author: gerardo.cicalese@polimi.it

# 1 Introduction

Since the early 1990s, numerous architects and building designers have begun utilizing acoustic simulation software to anticipate specific objective acoustical parameters during the room design phase. However, many errors have arisen due to overreliance on acoustical quality indices like clarity and strength, which fail to grasp the intricacies of environmental acoustic features. Auralizations were introduced to address challenges, enabling individuals to audibly experience how a designed room sounds before construction through numerical simulations, and facilitating subjective evaluation of acoustic design quality.

The emergence of acoustic virtual reality (AVR) is notable: equipped with a virtual reality headset, users can navigate simulated environments to experience the predicted acoustic ambiance. This enables straightforward assessment of spatial acoustic variations and the effects of changing parameters (e.g., altering wall materials or rearranging furniture), streamlining the design process. For a dynamic scene-compatible auralization algorithm, readers are referred to [7]. Given that acoustic is influenced by source/receiver placement and other geometry or material parameters, AVR necessitates continuous acoustic simulations, which can be computationally demanding. In the literature, we find two primary approaches to acoustics simulation: geometrical and wave-based methods. See, e.g., [22, 4]. Geometrical methods prove highly efficient in simulating room acoustics; however, since their simplified assumptions, they fail to capture numerous acoustic phenomena, especially at low frequencies, despite their minimal computational demands. On the other hand, wave-based methods approximate partial differential equations, inherently capturing all wave phenomena, albeit at a higher computational cost that increases with frequency [17].

The Adaptive Rectangular Decomposition (ARD), introduced by [19] and developed successively in [20, 21, 16, 18, 5], is a wave-based simulation algorithm noted for its accuracy and computational efficiency, which also incorporates support for absorbing boundary conditions via Perfectly Matched Layers (PML). Nevertheless, it possesses inherent limitations such as the absence of atmospheric absorption modeling which is addressed in this study. To explain the fundamentals of ARD, we report the pioneering algorithm presented in [19] that is based on the following steps: (i) the domain is voxelized into a uniform grid with spacing $dh$; (ii) the grid is partitioned into rectangular subdomains; (iii) assuming homogeneous Neumann boundary conditions, modal analysis is performed in each subdomain to retrieve the mode shapes and modal frequencies; (iv) a transformation is built to move from the modal-time domain to the space-time domain and back. The governing equation considered in each rectangular subdomain is the wave equation which is discretized in space employing a finite-difference method,

resulting in a system of coupled ordinary differential equations (ODE) in time. Then, the ODE system is solved in the modal space through the transformation in (iii), obtaining a system of independent ODE in time. These ODEs are solved using a Finite-Difference Time-Domain (FDTD) scheme, and the solution is transformed back to the spatial domain. The solutions obtained in each subdomain are corrected (interface handling step) to impose the propagation of sound waves between all the subdomains sharing an internal interface.
In [20], ARD is presented as an improvement of the previously described method. In particular (a) the ODE system is solved using an exact discretization scheme presented in [8] which, unlike the previously employed FDTD scheme, is unconditionally stable and does not introduce numerical dispersion; (b) the transformation between modal-time and space-time domain is replaced by the Discrete Cosine Transform (DCT), which can be performed more efficiently. The benefits of ARD, according to [19] and [20], are the following:

- it encompasses all wave phenomena, such as diffraction and reflection, in contrast to geometrical methods;
- even as the grids approach the Nyquist limit, its accuracy remains intact. In contrast, many wave-based methods demand grids with at least 5 points per wavelength to minimize dispersion, resulting in heightened computational and memory efficiency;
- it can be easily coupled with other simulation methods;
- it can be easily parallelized: all the subdomains can be updated independently (coarse-grained parallelism), and all the cells in modal subdomains can be updated independently (fine-grained parallelism). Refer to [15] for further details.

We refer to [14] for application/validation of the ARD scheme in scenarios involving the scattering of spherical waves by a rigid sphere and edge diffraction from a right-angled rigid wall. Furthermore, ARD is employed to predict acoustic propagation in a test urban (outdoor) environment, and the agreement with measurement data is reported to be better than the results obtained with the FDTD method in 2D [14]. In [1], the validation of ARD was conducted within a selected architectural setting, encompassing both indoor and outdoor scenarios. The findings revealed a close correspondence between the simulated decay profile generated by ARD and the measured data. Notably, ARD accurately anticipated mitigating flutter echoes when certain walls were tilted. In [16] a novel efficient parallelization or the ARD algorithm is proposed to improve computational efficiency and obtain scalable performance on distributed architectures. [18] use the ARD algorithm to simulate sound propagation in a confined environment while accurately taking account of the acoustic scattering and diffraction effects

generated by the presence of geometrical relief on the room surfaces. Finally, [5] try to accelerate the simulations using the ARD algorithm coupled with the spectral element method near the boundaries to handle complex geometries with realistic boundaries.
Despite these important applications, one of the main limitations of ARD is the lack of atmospheric absorption modeling. The attenuation of sound waves in the free medium becomes significant in large rooms, particularly at high frequencies [12]. Hence, to achieve realistic room acoustic simulations, emulation of air absorption is critical [11]. In this work, we introduce frequency-dependent damping to model viscous dissipation in the air. By following [8] we extend, generalize, and analyze the ARD algorithm for this case. The remaining of the paper is organized as follows. In Section 2 we introduce the mathematical model and derive the ARD method by introducing the necessary methodology, i.e., the Finite-Difference Time Domain (FDTD), the Fourier, and the Rectangular Domain Decomposition (RDD) methods. We also briefly discuss their stability properties. Next, we generalize the RDD to domains of arbitrary shape with partial absorbing boundaries. In Section 3, we first verify the scheme against manufactured solutions and then, in Section 4, we apply the scheme to a case of engineering interest.

## 2 Model problem and numerical discretization

In this section, we introduce the model problem and present the discretization technique that will be employed extensively in this work.

### 2.1 Acoustic problem formulation

The propagation of sound waves in an isentropic fluid within a three-dimensional domain $\Omega = [0,\ell_x]\times[0,\ell_y]\times[0,\ell_z]$ is characterized by the (viscous) *acoustic wave equation*:

$$\begin{cases} \dfrac{\partial^2 p}{\partial t^2}(\underline{x},t) + 2\alpha \dfrac{\partial p}{\partial t}(\underline{x},t) - c^2\Delta p(\underline{x},t) = f(\underline{x},t), & t\in\mathbb{R}^+,\ \ \underline{x}\in\Omega,\\ \dfrac{\partial p}{\partial \underline{n}}(\underline{x},t)=0, & t\in\mathbb{R}^+,\ \ \underline{x}\in\partial\Omega,\\ \left(p,\dfrac{\partial p}{\partial t}\right)(\underline{x},0) = (p_0,v_0)(\underline{x}), & \underline{x}\in\Omega,\end{cases} \tag{1}$$

where $p(\underline{x},t)$ denotes the pressure at point $\underline{x} = (x,y,z)$ at time $t$, $c$ is the *propagation speed*, $f(\underline{x},t)$ denotes an external force, and $\alpha \geq 0$ is the *absorption coefficient*. In (1) $p_0$ and $v_0$ are given functions representing arbitrary initial conditions. The homogeneous Neumann boundary condition models a sound hard boundary. By introducing the pressure velocity $v$ we can reformulate (1) as

$$
\begin{cases}
\dfrac{\partial v}{\partial t}(\underline{x},t) + 2\alpha v(\underline{x},t) - c^2 \Delta p(\underline{x},t) = f(\underline{x},t), & t \in \mathbb{R}^+, \underline{x} \in \Omega, \\
\dfrac{\partial p}{\partial t}(\underline{x},t) = v(\underline{x},t), & t \in \mathbb{R}^+, \underline{x} \in \Omega, \\
\dfrac{\partial p(\underline{x},t)}{\partial \underline{n}} = 0, & t \in \mathbb{R}^+, \underline{x} \in \partial\Omega, \\
(p,v)(\underline{x},0) = (p_0,v_0)(\underline{x}), & \underline{x} \in \Omega.
\end{cases}
\tag{2}
$$

## 2.2 Finite-Difference Time-Domain method (FDTD)

To find an approximated solution to problem (2) we define a space-time grid (staggered in space) with constant space step size $dh$ and constant time step $dt$:

$$
\begin{aligned}
x_i &= \left(i + \frac{1}{2}\right) \cdot dh, & i &\in D_x = \{0, \dots, L_x - 1\}, \\
y_j &= \left(j + \frac{1}{2}\right) \cdot dh, & j &\in D_y = \{0, \dots, L_y - 1\}, \\
z_k &= \left(k + \frac{1}{2}\right) \cdot dh, & k &\in D_z = \{0, \dots, L_z - 1\}, \\
t^n &= n \cdot dt, & n &\in \mathbb{N},
\end{aligned}
$$

with $L_w = \ell_w/dh - 1$ for $w = \{x,y,z\}$. We store the discretized functions in vectors with a row-major order: $D = \Big\{m = i + jL_x + kL_xL_y \mid i \in D_x,\ j \in D_y,\ k \in D_z\Big\} = \{0, \dots, L-1\}$, where $L = L_xL_yL_z$. Next, for any $m \in D$ and any $n \in \mathbb{N}$, we introduce the notation

$$
\varphi^n_m = \varphi^n_{i,j,k} = \varphi(x_i, y_j, z_k, t^n),
$$

and define the vector $\underline{\varphi}^n_{:,j,k}$ to denote the restriction of $\varphi$ to the line parallel to the $x$ axis and passing through the point $(x_0, y_j, z_k)$, for $\varphi \in \{p, v, f\}$. In the same way, we define $\underline{\varphi}^n_{i,:,k}$ and $\underline{\varphi}^n_{i,j,:}$. To reduce dispersion errors in the finite-difference scheme, as suggested in [20], we approximate $\Delta p$ in (2) using the $19-$points centered stencil

$$
(\Delta p)^n_{i,j,k} = \frac{1}{dh^2} \sum_{\ell=-3}^{3} \left( a_h p^n_{i+\ell,j,k} + a_h p^n_{i,j+\ell,k} + a_h p^n_{i,j,k+\ell} \right),
$$

where the coefficients are given by $a_{-3} = a_3 = 1/90$, $a_{-2} = a_2 = -3/20$, $a_{-1} = a_1 = 3/2$, and $a_0 = -49/18$. To impose Neumann boundary conditions we modify the scheme by imposing even symmetry in a standard manner [13]. Then, to integrate in time equations in (2), we employ the explicit scheme

$$
\begin{cases}
p^{n+1}_m = dt v^n_m + p^n_m, & n \in \mathbb{N}, m \in D, \\
v^{n+1}_m = \dfrac{v^n_m + c^2 dt (\Delta p)^{n+1}_m + dt f^{n+1}_m}{1 + 2dt\alpha}, & n \in \mathbb{N}, m \in D, \\
(\underline{p}^0, \underline{v}^0) = (\underline{p}_0, \underline{v}_0),
\end{cases}
\tag{3}
$$

where $\underline{p}_0$ and $\underline{v}_0$ are vectors storing the initial pressure and pressure velocity conditions at the grid points.

**Proposition 1** (Stability of the FDTD scheme (3))**.** *Scheme (3) is stable provided that the following Courant-Friedrichs-Lewy (CFL) condition is satisfied:*

$$c\frac{dt}{dh} \leq \frac{\sqrt{255}}{34} \approx 0.47. \tag{4}$$

*Proof.* We start by rewriting the first two equations in (3):

$$\begin{bmatrix} \underline{v} \\ \underline{p} \end{bmatrix}^{n+1} = [S_{FD}]_{2L} \begin{bmatrix} \underline{v} \\ \underline{p} \end{bmatrix}^{n} + \begin{bmatrix} dt\underline{f}^{n+1} \\ \underline{0} \end{bmatrix}, \tag{5}$$

where $[S_{FD}]_{2L} \in \mathbb{R}^{2L\times 2L}$ is defined as

$$[S_{FD}]_{2L} = \begin{bmatrix} \dfrac{[I]_L + c^2\frac{dt^2}{dh^2}[K]_L}{1+2dt\alpha} & \dfrac{c^2\frac{dt}{dh^2}[K]_L}{1+2dt\alpha} \\ dt[I]_L & [I]_L \end{bmatrix},$$

with $[I]_L$ the identity matrix in $\mathbb{R}^{L\times L}$ and $[K]_L \in \mathbb{R}^{L\times L}$ defined as

$$[K]_L = [I]_{L_z} \otimes [I]_{L_y} \otimes [K]_{L_x} + [I]_{L_z} \otimes [K]_{L_y} \otimes [I]_{L_x} + [K]_{L_z} \otimes [I]_{L_y} \otimes [I]_{L_x},$$

being $\otimes$ the Kronecker product. The matrices $[I]_{L_w}$, for $w = \{x, y, z\}$ are identity matrices of dimension $L_w \times L_w$ while $[K]_{L_w}$, for $w = \{x, y, z\}$ are heptadiagonal matrices having size $L_w \times L_w$ and are defined as

$$[K]_{L_w} = \begin{bmatrix} a_0+a_1 & a_1+a_2 & a_2+a_3 & a_3 & 0 & 0 & 0 & 0 & \dots \\ a_1+a_2 & a_0+a_3 & a_1 & a_2 & a_3 & 0 & 0 & 0 & \dots \\ a_2+a_3 & a_1 & a_0 & a_1 & a_2 & a_3 & 0 & 0 & \dots \\ a_3 & a_2 & a_1 & a_0 & a_1 & a_2 & a_3 & 0 & \dots \\ 0 & a_3 & a_2 & a_1 & a_0 & a_1 & a_2 & a_3 & \dots \\ \vdots & \vdots & \vdots & \vdots & \vdots & \vdots & \vdots & \vdots & \ddots \end{bmatrix}.$$

To prove the stability of (5) we compute the spectral radius $\sigma_{S_{FD}}$ of $[S_{FD}]_{2L}$ and check if it is less than or equal to 1, i.e., $\sigma_{S_{FD}} \leq 1$. Let us start by considering the case $\alpha = 0$ and observing that the eigenvalues $\lambda_{S_{FD}}$ of $[S_{FD}]_{2L}$ are given by

$$\lambda_{S_{FD}}^2 - \left(2 + \lambda_K \left(c\frac{dt}{dh}\right)^2\right)\lambda_{S_{FD}} + 1 = 0,$$

being $\lambda_K$ an eigenvalue of $[K]_L$. It can be shown that $|\lambda_{S_{FD}}| = 1$ if the discriminant is non-positive, i.e.,

$$\left(\frac{1}{2}\lambda_K\left(c\frac{dt}{dh}\right)^2\right) + \lambda_K\left(c\frac{dt}{dh}\right)^2 \leq 0.$$

This condition is satisfied if and only if $|\lambda_K| \leq 4/\left(c\frac{dt}{dh}\right)^2$ for any $\lambda_K$. This is equivalent to requiring that the spectral radius $\sigma_K$ of $[K]_L$ is $\sigma_K \leq 4/\left(c\frac{dt}{dh}\right)^2$, that is $c\frac{dt}{dh} \leq \frac{2}{\sqrt{\sigma_K}}$. From the Gershgorin's theorem [3] it follows that

$$\sigma_K = 3\sum_{i=-3}^{3}|a_i| = \frac{272}{15},$$

hence $c\frac{dt}{dh} \leq \frac{\sqrt{255}}{34}$. The proof for the case $\alpha > 0$ is analogous (despite being longer) and omitted here for brevity: it can be shown that (4) is a lower bound for a less restrictive CFL condition. □

## 2.3 Fourier method

In this section, based on the work by [19], [20] and [23], we modify the classical Fourier method to support air absorption. We start by introducing the following mode shapes, cf. [2],

$$q_{\mu\nu\xi}(\underline{x}) = \sqrt{\frac{8}{\ell_x\ell_y\ell_z}}\varepsilon_\mu\varepsilon_\nu\varepsilon_\xi \cos\left(\frac{\mu\pi}{\ell_x}x\right)\cos\left(\frac{\nu\pi}{\ell_y}y\right)\cos\left(\frac{\xi\pi}{\ell_z}z\right), \tag{6}$$

where $\varepsilon_0 = \frac{1}{\sqrt{2}}$, and $\varepsilon_\mu = 1$ for $\mu > 0$, and express $p(\underline{x}, t)$ as a linear combination of the mode shapes

$$p(\underline{x}, t) = \sum_{\xi=0}^{\infty}\sum_{\nu=0}^{\infty}\sum_{\mu=0}^{\infty} P_{\mu\nu\xi}(t)q_{\mu\nu\xi}(\underline{x}), \tag{7}$$

where the modal coefficients $P_{\mu\nu\xi}(t)$ can be computed as

$$P_{\mu\nu\xi}(t) = \int_0^{\ell_z}\int_0^{\ell_y}\int_0^{\ell_x} p(\underline{x}, t)q_{\mu\nu\xi}(\underline{x})dxdydz. \tag{8}$$

Next, we do the same for $f$ and $v$ to obtain $F_{\mu\nu\xi}$ and $V_{\mu\nu\xi}$. Then, we reformulate problem (1) for $t \in \mathbb{R}^+$, $\mu$, $\nu$, $\xi \in \mathbb{N}^+$, (1) as

$$\begin{cases} \ddot{P}_{\mu\nu\xi}(t) + 2\alpha\dot{P}_{\mu\nu\xi}(t) + \omega^2_{0;\mu\nu\xi}P_{\mu\nu\xi}(t) = F_{\mu\nu\xi}(t), \\ (P_{\mu\nu\xi}, \dot{P}_{\mu\nu\xi})(0) = (P_{\mu\nu\xi,0}, V_{\mu\nu\xi,0}), \end{cases} \tag{9}$$

where $P_{\mu\nu\xi,0}, V_{\mu\nu\xi,0}$ are given coefficients representing arbitrary initial conditions, and $\omega_{0;\mu\nu\xi} = c\pi\sqrt{\frac{\mu^2}{\ell_x^2} + \frac{\nu^2}{\ell_y^2} + \frac{\xi^2}{\ell_z^2}}$. We notice that, for each tuple $(\mu, \nu, \xi)$, (9) represents the equation of motion for a single degree-of-freedom system (forced damped harmonic oscillator). Employing the staggered space grid defined in Sec. 2.2, we rewrite the mode shapes in (6) as

$$q_{\mu\nu\xi,ijk} = \sqrt{\frac{8}{L_x L_y L_z}}\varepsilon_\mu \varepsilon_\nu \varepsilon_\xi \cos\left(\frac{\pi\mu}{L_x}\left(i+\frac{1}{2}\right)\right)\cos\left(\frac{\pi\nu}{L_y}\left(j+\frac{1}{2}\right)\right)\cos\left(\frac{\pi\xi}{L_z}\left(k+\frac{1}{2}\right)\right).$$

Notice that, since we are dealing with discrete signals in space, the spatial frequencies are limited by the Nyquist frequency. E.g., considering for example the $x$ axis, we have that $\frac{\pi\mu}{L_x} < \pi \implies \mu < L_x$. Hence, $\mu \in D_x$, $\nu \in D_y$, and $\xi \in D_z$. Recalling (7), we express $p_m(t)$ as

$$p_m(t) = \sum_{\eta=0}^{L-1} q_{\eta,m} P_\eta(t), \tag{10}$$

where $P_\eta$ are the modal coefficients of the pressure $p$. Conversely, recalling (8), the modal coefficients $P_\eta(t)$ can be computed through

$$P_\eta(t) = \sum_{m=0}^{L-1} q_{\eta,m} p_m(t). \tag{11}$$

The same can be done for the force $f$ and the pressure velocity $v$. Notice that (11) corresponds to the Discrete Cosine Transform (DCT) in its DCT-II form, while (10) corresponds to the inverse DCT in its DCT-III form [6]. To conclude, we reformulate problem (9) as

$$\begin{cases} \ddot{P}_\eta(t) + 2\alpha\dot{P}_\eta(t) + \omega_{0;\eta}^2 P_\eta(t) = F_\eta(t), \quad t \in \mathbb{R}^+, \eta \in D, \\ (\underline{P}, \dot{\underline{P}})(0) = (\underline{P}_0, \underline{V}_0), \end{cases} \tag{12}$$

or in its first-order variant

$$\begin{cases} \begin{bmatrix} \dot{V}_\eta(t) \\ \dot{P}_\eta(t) \end{bmatrix} = \begin{bmatrix} -2\alpha & -\omega_{0;\eta}^2 \\ 1 & 0 \end{bmatrix} \begin{bmatrix} V_\eta(t) \\ P_\eta(t) \end{bmatrix} + \begin{bmatrix} F_\eta(t) \\ 0 \end{bmatrix}, \quad t \in \mathbb{R}^+, \eta \in D, \\ (\underline{P}(0), \underline{V}(0)) = (\underline{P}_0, \underline{V}_0). \end{cases} \tag{13}$$

Following the idea presented in [8], to integrate in time system (13), we consider the general scheme

$$\begin{bmatrix} V_\eta \\ P_\eta \end{bmatrix}^{n+1} = [S_\eta] \begin{bmatrix} V_\eta \\ P_\eta \end{bmatrix}^n + [T_\eta] F_\eta^n, \quad \text{for } n \geq 0. \tag{14}$$

The definition of the matrices $[S_\eta]$ and $[T_\eta]$ depend on the four cases:

i) $\eta = 0$ and $\alpha = 0$,

$$[S_0] = \begin{bmatrix} 1 & 0 \\ dt & 1 \end{bmatrix}, \quad [T_0] = \begin{bmatrix} dt \\ \dfrac{dt^2}{2} \end{bmatrix},$$

ii) $\eta = 0$ and $\alpha > 0$,

$$[S_0] = \begin{bmatrix} e^{-2\alpha dt} & 0 \\ \dfrac{1 - e^{-2\alpha dt}}{2\alpha} & 1 \end{bmatrix}, \quad [T_0] = \begin{bmatrix} \dfrac{1 - e^{-2\alpha dt}}{2\alpha} \\ \dfrac{e^{-2\alpha dt} - 1}{4\alpha^2} + \dfrac{1}{2\alpha} dt \end{bmatrix},$$

iii) $\eta > 0$ and $0 \leq \alpha < \omega_{0;\eta}$,

$$[S_\eta] = e^{-\alpha dt} \cos(\omega_\eta dt) \begin{bmatrix} 1 & 0 \\ 0 & 1 \end{bmatrix} + e^{-\alpha dt} \sin(\omega_\eta dt) \begin{bmatrix} -\dfrac{\alpha}{\omega_\eta} & -\left(\omega_\eta + \dfrac{\alpha^2}{\omega_\eta}\right) \\ \dfrac{1}{\omega_\eta} & \dfrac{\alpha}{\omega_\eta} \end{bmatrix},$$

$$[T_\eta] = -\frac{1}{\omega_{0;\eta}^2} \begin{bmatrix} e^{-\alpha dt} \left(\omega_\eta + \dfrac{\alpha^2}{\omega_\eta}\right) \sin(\omega_\eta dt) \\ 1 - e^{-\alpha dt} \left(\cos(\omega_\eta dt) + \dfrac{\alpha}{\omega_\eta} \sin(\omega_\eta dt)\right) \end{bmatrix},$$

where $\omega_\eta = \sqrt{\omega_{0;\eta}^2 - \alpha^2}$ are the damped frequencies.

iv) $\eta > 0$ and $\alpha > \omega_{0;\eta}$,

$$[S_\eta] = \frac{1}{2} \begin{bmatrix} \left(e^{-\alpha_{1;\eta} dt} + e^{-\alpha_{2;\eta} dt}\right) & -\left(\alpha_{1;\eta} e^{-\alpha_{1;\eta} dt} + \alpha_{2;\eta} e^{-\alpha_{2;\eta} dt}\right) \\ 0 & 2\left(e^{-\alpha_{1;\eta} dt} + e^{-\alpha_{2;\eta} dt}\right) \end{bmatrix}$$

$$+ \frac{1}{2\alpha_{d;\eta}} \begin{bmatrix} \alpha\left(e^{-\alpha_{1;\eta} dt} - e^{-\alpha_{2;\eta} dt}\right) & -\alpha\left(\alpha_{2;\eta} e^{-\alpha_{2;\eta} dt} - \alpha_{1;\eta} e^{-\alpha_{1;\eta} dt}\right) \\ \left(e^{-\alpha_{2;\eta} dt} - e^{-\alpha_{1;\eta} dt}\right) & \left(\alpha_{2;\eta} e^{-\alpha_{2;\eta} dt} - \alpha_{1;\eta} e^{-\alpha_{1;\eta} dt}\right) \end{bmatrix},$$

$$[T_\eta] = \frac{1}{\omega_{0;\eta}^2} \begin{bmatrix} \dfrac{1}{2}\left(\alpha_{1;\eta} e^{-\alpha_{1;\eta} dt} + \alpha_{2;\eta} e^{-\alpha_{2;\eta} dt} + \dfrac{\alpha}{\alpha_{d;\eta}}\left(\alpha_{2;\eta} e^{-\alpha_{2;\eta} dt} - \alpha_{1;\eta} e^{-\alpha_{1;\eta} dt}\right)\right) \\ 1 - e^{-\alpha_{1;\eta} dt} - e^{-\alpha_{2;\eta} dt} - \dfrac{1}{2\alpha_{d;\eta}}\left(\alpha_{2;\eta} e^{-\alpha_{2;\eta} dt} - \alpha_{1;\eta} e^{-\alpha_{1;\eta} dt}\right) \end{bmatrix},$$

where and $\alpha_{d;\eta} = \sqrt{\alpha^2 - \omega_{0;\eta}^2}$, $\alpha_{1,2;\eta} = \alpha \pm \alpha_{d;\eta}$.

**Proposition 2** (Stability of the Fourier method)**.** *Scheme* (14) *is unconditionally stable.*

*Proof.* For each of the four cases, we compute the eigenvalues of $[S_\eta]$ and check that their absolute value is less than or equal to $1$.

i) It is easy to check that $|\lambda_{1,2}| = 1$.

ii) Similarly, we have $|\lambda_1| = e^{-2\alpha dt} < 1$ and $|\lambda_2| = 1$.

iii) For $\alpha = 0$, the characteristic equation is

$$|[S_\eta] - \lambda[I]| = \lambda^2 - 2\lambda \cos(\omega_\eta dt) + 1 = 0.$$

Hence, $\lambda_{1,2} = \cos(\omega_\eta dt) \pm \jmath \sin(\omega_\eta dt)$ and then $|\lambda_{1,2}| = 1$. Similar result holds for $0 < \alpha < \omega_{0;\eta}$.

iv) In this case, it can be proven that

$$\lambda_1 = e^{-dt\left(\alpha + \sqrt{\alpha^2 - \omega_{0;\eta}^2}\right)}, \quad \lambda_2 = e^{-dt\left(\alpha - \sqrt{\alpha^2 - \omega_{0;\eta}^2}\right)},$$

so that $|\lambda_{1,2}| < 1$ for each value of $\alpha > \omega_{0;\eta}$.

□

## 2.4 Rectangular Domain Decomposition

The Fourier method presented in Sec. 2.3 is not suited for complex geometries: indeed, it is valid only for parallelepipedal domains. To overcome this limitation. the Rectangular Domain Decomposition (RDD) has been introduced and employed in the literature [19, 20, 23]. Here, for the sake of completeness, we briefly review the main aspects of RDD considering the case where $\Omega$ is a parallelepiped of dimension $2\ell_x, \ell_y$, and $\ell_z$ as represented in Fig. 1, and adapt it to handle the discretization in Section 2.2.

### 2.4.1 Derivation of RDD for the FDTD scheme and extension to the Fourier method

We consider a staggered uniform spatial grid of step size $dh$ along all directions as follows:

$$\begin{aligned} x_i &= \left(i + \frac{1}{2}\right) \cdot dh, \quad i \in D_x = \{0, \dots, 2L_x - 1\}, \\ y_j &= \left(j + \frac{1}{2}\right) \cdot dh, \quad j \in D_y = \{0, \dots, L_y - 1\}, \\ z_k &= \left(k + \frac{1}{2}\right) \cdot dh, \quad k \in D_z = \{0, \dots, L_z - 1\}. \end{aligned}$$

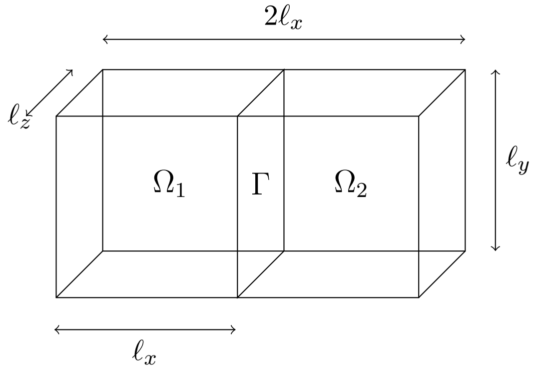

Figure 1: Representation of the domain $\Omega$ partitioned into two non-overlapping subdomains $\Omega_1, \Omega_2$, sharing the interface $\Gamma$.

We store the grid functions in vectors with a row-major order

$$D = \Big\{ m = i + j2L_x + k2L_xL_y \mid i \in D_x, j \in D_y, k \in D_z \Big\} = \{0, \ldots, 2L-1\},$$

where $L = L_xL_yL_z$, and consider the first-order FDTD scheme (3). For the sake of presentation, we partition the domain $\Omega$ into two distinct non-overlapping subdomains: $\Omega_1$, corresponding to $x \leq \ell_x$, and $\Omega_2$, corresponding to $x \geq \ell_x$. These subdomains have dimensions $\ell_x$, $\ell_y$, and $\ell_z$, as illustrated in Figure 1, and they share the interface $\Gamma$, which is a surface parallel to the $yz$ plane. We use the subscript $d$ to denote a quantity in the subdomain $\Omega_d$, $d = 1, 2$, and use the notation

$$\varphi^n_{i,j,k;d} = \varphi(x_i, y_j, z_k, t^n), \quad \text{for} \quad (x_i, y_j, z_k) \in \Omega_d,$$

with $\varphi = \{p, v, f\}$. We proceed by decoupling the matrix $[K]_{2L_x}$ of dimensions $2L_x \times 2L_x$ into a block-diagonal form matrix $[A]_{2L_x}$ and a residual matrix $[C]_{2L_x}$:

$$[K]_{2L_x} = [A]_{2L_x} + [C]_{2L_x},$$

where

$$[A]_{2L_x} = \begin{bmatrix} [K]_{L_x} & [0]_{L_x} \\ [0]_{L_x} & [K]_{L_x} \end{bmatrix},$$

and $[C]_{2L_x}$ is computed by difference. We can interpret the matrix $[A]_{2L_x}$ as imposing the homogeneous Neumann boundary conditions (even symmetry) at the interface $\Gamma$, while the matrix $[C]_{2L_x}$ as imposing the transmission conditions. We introduce the *residual* $r^{n+1}_{i,j,k}$, defined as

$$\underline{r}^{n+1}_{:,j,k} = \left(\frac{c}{dh}\right)^2 [C]_{2L_x}\, \underline{p}^{n+1}_{:,j,k}, \quad n \in \mathbb{N}, \;\; j \in D_y, \;\; k \in D_z. \tag{15}$$

Notice that the residual cannot be computed independently in each subdomain, as it depends also on the pressure in the neighboring region. However, as the matrix $[C]_{2L_x}$ is sparse, only $6$ pressure values are considered at positions $L_x - 3, L_x - 2$, and $L_x - 1$ for $\Omega_1$ and at positions $0, 1$, and $2$ for $\Omega_2$. With this formalism, the FDTD scheme (3) can be rewritten as

$$\begin{cases} p_{i,j,k;d}^{n+1} = dt v_{i,j,k;d}^{n} + p_{i,j,k;d}^{n}, \\ \widehat{v}_{i,j,k;d}^{n+1} = \dfrac{v_{i,j,k;d}^{n} + c^2 dt (\Delta p)_{i,j,k;d}^{n+1} + dt f_{i,j,k;d}^{n+1}}{1 + 2dt\alpha}, \\ (\underline{p}_d^0, \underline{v}_d^0) = (\underline{p}_{d;0}, \underline{v}_{d;0}), \end{cases} \tag{16}$$

for $n \in \mathbb{N}, i \in D_d, j \in D_y, k \in D_z$, and $d = 1, 2$. We then use the residual (15) to correct the solution given by (16) near the interfaces:

$$v_{i,j,k}^{n+1} \leftarrow \widehat{v}_{i,j,k}^{n+1} + \frac{dt}{1 + 2dt\alpha} r_{i,j,k}^{n+1}. \tag{16.a}$$

We refer to the last step as *interface correction step*. This technique can be combined with the Fourier method introduced in Section 2.3. Indeed, one can apply the scheme (14) to compute the solution in each subdomain $\Omega_d$, $d = 1, 2$ and use the residual (16.a) to update it near the interfaces. In this case, the coupling is not exact, as the residual is built on the FDTD method. This introduces erroneous (spurious) reflections at the interface between subdomains, grid dispersion, and a restriction on the simulation time step given by (4). The latter result comes from [14, 15], which suggest that the CFL condition of the ARD corresponds to that of the FDTD scheme employed to derive the residual.

#### 2.4.2 Generalization of RDD for domains of arbitrary shape with partial absorbing boundaries

In this section, we explain how to generalize the scheme introduced previously for the case of arbitrarily shaped domains with partial absorbing boundaries. The model introduces the latter through perfectly matched layer (PML) conditions. For presentation sake, we detail the implementation of PML conditions in Appendix A. As proposed in [20] partial boundary absorption is treated by modifying the interface correction step:

$$v_{i,j,k}^{n+1} \leftarrow \widehat{v}_{i,j,k}^{n+1} + \beta \frac{dt}{1 + 2dt\alpha} r_{i,j,k}^{n+1},$$

where $0 \leq \beta \leq 1$ is the dimensionless boundary absorption coefficient (e.g., full reflection with $\beta = 0$ or full absorption with $\beta = 1$). This scheme, called Adaptive Rectangular Decomposition (ARD), consists of two primary stages:

- *Preprocessing* (Fig. 4).

1) The input scene is voxelized into grid cells at grid resolution $dh$.
2) The grid cells are grouped into $N_d$ rectangles corresponding to air subdomains $\Omega_d$, for $d = 1, ..., N_d$, and PML subdomains $\Omega_{PML}$ are generated for each boundary. For each $\Omega_d$ we store the grid functions and other variables needed to run the solution scheme.
3) The interfaces between adjacent subdomains are created by examining adjacency relationships.

- *Simulation loop*.

1) For each subdomain $\Omega_d$, we update the solution by employing the Fourier method in Section 2.3, and the FDTD scheme described in Section A for PML subdomains. The chosen time step $dt$ must satisfy (4).
2) For each interface, we perform the interface correction step.

## 3 Numerical results

In this section, we perform numerical experiments to validate the efficiency of the proposed scheme (14), either with or without the interface correction step (16.a), in terms of convergence, accuracy, and efficiency.

### 3.1 Fourier method

In this section, we perform some convergence tests for the scheme (14). We consider a domain $\Omega = (0, 10 \text{ m})^3$, with propagation speed $c = 1$ m/s, and the following standing wave solution associated to mode $(\mu, \nu, \xi) = (7, 2, 2)$:

$$p(x, y, z, t) = \cos\left(\frac{7\pi}{10}x\right)\cos\left(\frac{2\pi}{10}y\right)\cos\left(\frac{2\pi}{10}z\right)e^{-\alpha t}\cos(\omega t), \tag{17}$$

where $\omega = \sqrt{\omega_0^2 - \alpha^2}$ rad/s and $\omega_0 = \dfrac{\sqrt{57}}{10}c\pi$ rad/s. The $L^\infty$ error at the final time $T = 0.1$ s is computed as $\text{Err}_{L^\infty}(T) = \max_{x_i, y_j, z_k \in \Omega} |p_h(x_i, y_j, z_k, T) - p(x_i, y_j, z_k, T)|$, where $p_h$ represents the numerical solution, $p$ is the analytical solution in (17). Tables 1 and 2 summarize the computed $L^\infty$ error for different choices of $dh$ and $dt$ and different values of the absorption coefficient $\alpha$. We notice how the error stays in the order of magnitude of the machine precision ($2.2204$e–16). This confirms that the Fourier method is exact in both space and time. The small numerical error is a consequence of the floating-point arithmetic.

| $dt$<br>$\alpha$ | $0.001$ | $0.002$ | $0.005$ | $0.01$ |
|---|---|---|---|---|
| 0 | 5.5927e−15 | 2.9560e−15 | 1.2768e−15 | 6.5226e−16 |
| $0.5\omega_0$ | 4.3993e−15 | 2.2204e−15 | 1.2629e−15 | 4.9960e−16 |
| $1.5\omega_0$ | 5.1070e−15 | 1.8874e−15 | 1.0825e−15 | 4.9960e−16 |

Table 1: Test case of section 3.1: computed $L^\infty$ error for the Fourier method (14) by varying $dt$ for $dh = 0.125$ and different values of $\alpha$.

| $dh$<br>$\alpha$ | $0.03125$ | $0.0625$ | $0.125$ | $0.25$ |
|---|---|---|---|---|
| 0 | 5.8287e−16 | 6.3838e−16 | 6.5226e−16 | 5.2736e−16 |
| $0.5\omega_0$ | 4.9960e−16 | 6.2450e−16 | 4.9960e−16 | 5.6899e−16 |
| $1.5\omega_0$ | 4.1633e−16 | 4.9960e−16 | 4.9960e−16 | 3.8858e−16 |

Table 2: Test case of section 3.1: computed $L^\infty$ error for the Fourier method (14) by varying $dh$ for $dt = 0.01$ and different values of $\alpha$.

### 3.2 Fourier method with RDD

In this section, we first perform a convergence test by combining the schemes (14) and (16.a), considering the same solution presented in the previous section with $\alpha = 0$. The domain $\Omega = (0, 10\text{ m})^3$ is partitioned into two subdomains as shown in Fig. 1: $\Omega_1 = (0, 5\text{ m}) \times (0, 10\text{ m})^2$ and $\Omega_2 = (5\text{ m}, 10\text{ m}) \times (0, 10\text{ m})^2$. We have chosen a test case suitable for assessing interface errors: a propagative solution. In this case, the propagation speed is $c = 5$ m/s, the prescribed initial velocity is zero, and the initial pressure is

$$p_0(x, y, z) = \frac{1}{(2\pi)^{3/2}\sigma_x\sigma_y\sigma_z} \exp\left(-\frac{1}{2}\left[\frac{(x-\mu_x)^2}{\sigma_x^2} + \frac{(y-\mu_y)^2}{\sigma_y^2} + \frac{(z-\mu_z)^2}{\sigma_z^2}\right]\right),$$

where $\mu_x = 2.5, \mu_y = \mu_z = 0.5$ and $\sigma_x = \sigma_y = \sigma_z = 0.5$. We obtain two waves: one traveling to the left and the other to the right of the domain. In Fig. 2, we plot the computed $L^\infty$ error at the final time $T = 1$ s for different choices of $dh$ and $dt$. We have chosen a longer simulation time to accentuate the interface errors. We conclude that the Fourier method with RDD converges to the ground truth solution with order $\mathcal{O}(dh + dt)$.

Then, in Fig. 3, we show the computed $L^\infty$ error in dB scale ($\text{Err}_{L^\infty}(T)$ dB $= 20\log_{10}(\text{Err}_{L^\infty}(T))$) by increasing the number of subdomains fixing $dh = 0.0625$ and $dt = 5.$e−3. We notice that the error increases slowly with the number of subdomains and can be considered inaudible

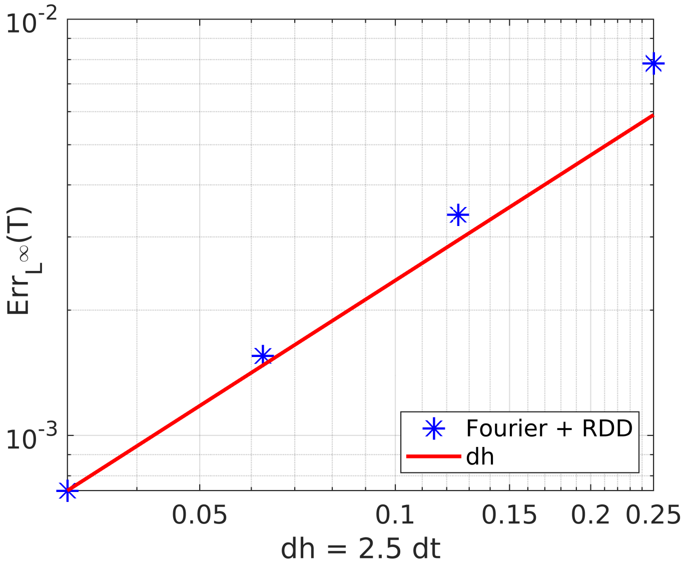

Figure 2: Test case of section 3.2: computed $L^\infty$ error at the final time $T = 1$ s for the Fourier method with RDD by varying $dh = 2.5dt$.

due to the acoustic masking phenomenon: the spurious reflections are masked by the incident waves, being the latter higher in loudness [9].

## 4 Application to room acoustics

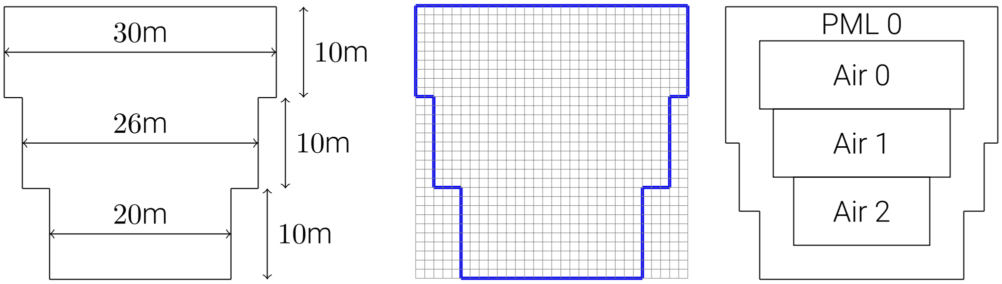

(a) Hall (domain). (b) Voxelization with $dh = 1$m. (c) Partitioning.

Figure 4: Preprocessing step of ARD in a test scenario (top view).

In this section, we test the previously derived ARD by enhancing the `c++` software *ARD-simulator* freely available on `https://github.com/jinnsjj/ARD-simulator` to include air absorption in the computational domain.

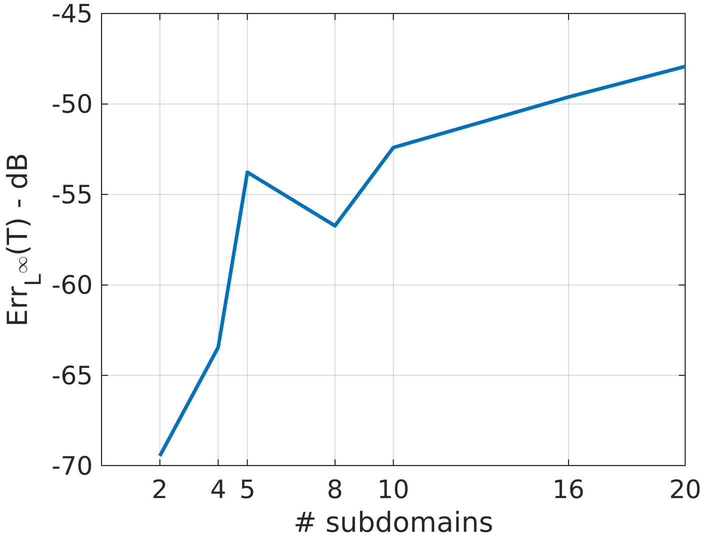

Figure 3: Test case of section 3.2: computed $L^\infty$ error at the final time $1$ s for Fourier method with RDD convergence test varying the number of subdomains.

This new version is available on `https://github.com/mazamin7/WASAbi`. We consider the simplified hall $\Omega$ depicted in Fig. 4(a) having a constant height of $10$ m, a volume of $7600$ m$^3$ and a surface area of $760$ m$^2$. We partition $\Omega$ into three rectangles, $\Omega_1$, $\Omega_2$ and $\Omega_3$ as shown in Fig. 4(c). We choose the propagation speed $c = 343.5$ m/s, the grid spacing $dh = 0.2$ m, the time step $dt = $ 2e$-$4 s, the boundaries absorption coefficient is $\beta = 0.5$ and the PML thickness is set to $5\ dh$. A visual comparison between the first case, where the air absorption coefficient is $\alpha = 0$, and the second case, where the air absorption coefficient is $\alpha = 10$, is shown in Fig. 5. The applied force is of the form $f(\underline{x}, t) = \delta(\underline{x} - \underline{x}_0)e^{-\left(\frac{t-t_0}{\sigma}\right)^2}$, where $\delta(\cdot)$ is the three-dimensional Dirac delta function, $\underline{x}_0$ is the position of the source, i.e., the center of the lower rectangle, $t_0 = 6dh/(cdt)$ and $\sigma = 3dh/(cdt)$. As expected, the solution obtained for the damped case is similar to the undamped one, except for the decaying pressure caused by air damping. This simulation, irrespective of the chosen physical parameters (speed of propagation, air and boundaries absorption), takes approximately $5$ minutes to simulate $0.1$ seconds of the event on a mid-range laptop (parallel computation on $8$ cores). With this example, we have demonstrated the applicability of this algorithm to realistic cases. We are convinced that its natively parallel structure will make it suitable for (almost) real-time simulations.

## 5 Conclusion

We have proposed an improved version of ARD which adds support for modeling atmospheric absorption, which leads to an increased simulation accuracy at higher frequencies, while not decreasing the computational efficiency and retaining all the other benefits (and the other limitations) of the original ARD presented in [20]. Future work could focus on rigorous mathematical analysis of the scheme convergence and accuracy, to ensure that the improved ARD method consistently provides reliable and precise results across different scenarios.

Further improvements in accuracy may involve developing an improved interface handling scheme that introduces less dispersion and reduces spurious reflections. Moreover, ARD could be embedded into a hybrid simulation technique to improve efficiency.

## 6 Acknowledgements

I. Mazzieri and G. Ciaramella are members of the INDAM GNCS.

## 7 Author declarations

The authors declare no conflicts of interest.

## 8 Data availability

The data supporting the findings of this study are available from the corresponding author upon reasonable request.

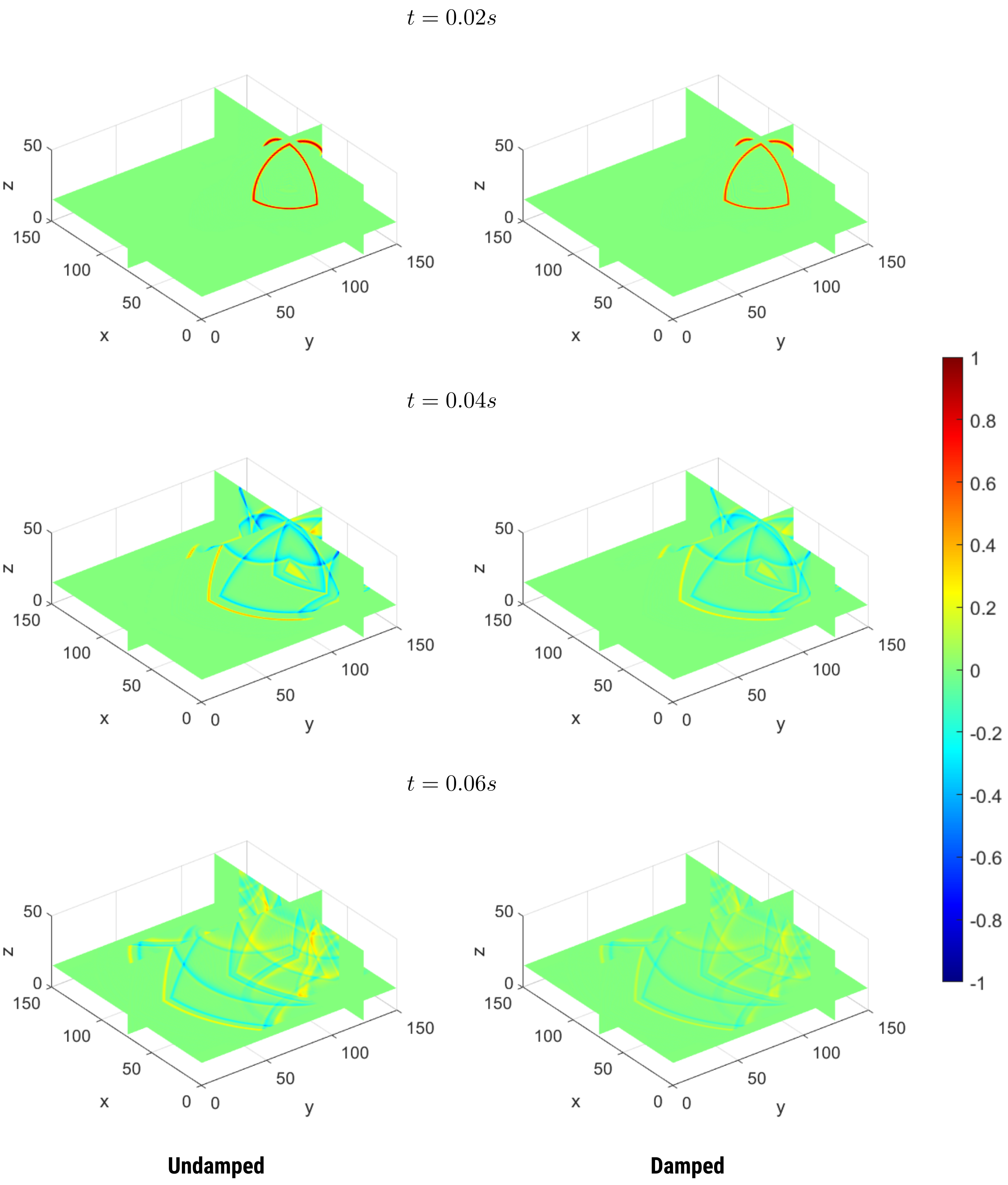

Figure 5: Comparison of undamped (column $1$) and damped case (column $2$) at different instants.

# 9 References

[1] L. Antani, A. Chandak, M. Wilkinson, A. A. Bassuet, and D. Manocha. Validation of adaptive rectangular decomposition for three-dimensional wave-based acoustic simulation in architectural models. In *Proceedings of Meetings on Acoustics*, volume 19. AIP Publishing, 2013.

[2] N. Asmar. *Partial Differential Equations with Fourier Series and Boundary Value Problems*. Pearson Prentice Hall, 2nd edition edition, 2005.

[3] H. E. Bell. Gershgorin's theorem and the zeros of polynomials. *The American Mathematical Monthly*, 72(3):292–295, 1965.

[4] D. R. Bergman. *Computational acoustics: theory and implementation*. John Wiley & Sons, 2018.

[5] N. Borrel-Jensen, A. P. Engsig-Karup, M. Hornikx, and C.-H. Jeong. Accelerated sound propagation simulations using an error-free Fourier method coupled with the spectral-element method. *Inter-Noise and Noise-Con Congress and Conference Proceedings*, 265(5):2731–2742, 2023.

[6] D. R. Bull and F. Zhang. *Intelligent image and video compression: communicating pictures*. Academic Press is an imprint of Elsevier, London, United Kingdom ; San Diego, CA, United States, second edition edition, 2021.

[7] A. Chandak, L. Antani, and D. Manocha. Efficient auralization for moving sources and receiver. In *Technical Report TR11-008, University of North Carolina at Chapel Hill. 127, 137*. 2011.

[8] J. L. Cieslinski. On the exact discretization of the classical harmonic oscillator equation. *Journal of Difference Equations and Applications*, 17(11):1673–1694, 2011.

[9] S. A. Gelfand. *Hearing: An introduction to psychological and physiological acoustics*. CRC Press, 2017.

[10] M. J. Grote and I. Sim. Efficient PML for the wave equation. *arXiv:1001.0319*, 2010.

[11] B. Hamilton. Adding air attenuation to simulated room impulse responses: A modal approach. In *2021 Immersive and 3D Audio: from Architecture to Automotive (I3DA)*, pages 1–10. IEEE, 2021.

[12] H. Kuttruff. *Room acoustics*. Spon Press/Taylor & Francis, London & New York, 5th ed edition, 2009.

[13] R. J. LeVeque. *Finite difference methods for ordinary and partial differential equations: steady-state and time-dependent problems*. SIAM, 2007.

[14] R. Mehra, N. Raghuvanshi, A. Chandak, D. Albert, D. Wilson, and D. Manocha. Validation of 3D numerical simulation for acoustic pulse propagation in an urban environment. *The Journal of the Acoustical Society of America*, 131:3333, 2012.

[15] R. Mehra, N. Raghuvanshi, L. Savioja, M. C. Lin, and D. Manocha. An efficient GPU-based time domain solver for the acoustic wave equation. *Applied Acoustics*, 73(2):83–94, 2012.

[16] N. Morales, R. Mehra, and D. Manocha. A parallel time-domain wave simulator based on rectangular decomposition for distributed memory architectures. *Applied Acoustics*, 97:104–114, 2015.

[17] F. Pind, C.-H. Jeong, H. S. Llopis, K. Kosikowski, and J. Strømann-Andersen. Acoustic virtual reality–methods and challenges. In *Proceedings of Baltic-Nordic Acoustic Meeting (BNAM), Reykjavík, Iceland*, 2018.

[18] K. Rabisse, J. Ducourneau, A. Faiz, and N. Trompette. Numerical modelling of sound propagation in rooms bounded by walls with rectangular-shaped irregularities and frequency-dependent impedance. *Journal of Sound and Vibration*, 440:291–314, 2019.

[19] N. Raghuvanshi, N. Galoppo, and M. C. Lin. Accelerated wave-based acoustics simulation. In *Proceedings of the 2008 ACM symposium on Solid and physical modeling*, pages 91–102, Stony Brook New York, 2008. ACM.

[20] N. Raghuvanshi, R. Narain, and M. C. Lin. Efficient and Accurate Sound Propagation Using Adaptive Rectangular Decomposition. *IEEE Transactions on Visualization and Computer Graphics*, 15(5):789–801, 2009.

[21] N. Raghuvanshi, J. Snyder, R. Mehra, M. Lin, and N. Govindaraju. Precomputed wave simulation for real-time sound propagation of dynamic sources in complex scenes. In *ACM Siggraph 2010 papers*, pages 1–11. 2010.

[22] L. Savioja, J. Huopaniemi, T. Lokki, and R. Väänänen. Creating Interactive Virtual Acoustic Environments. *Journal of the Audio Engineering Society*, 47(9):675–705, 1999.

[23] L. Savioja, D. Manocha, and M. Lin. Use of GPUs in room acoustic modeling and auralization. In *Proc. Int. Symposium on Room Acoustics*, page 3, 2010.

## A Implementation of Perfectly Matched Layer

To model partial absorption of the acoustic pressure on the boundaries of the computational domain we consider in the sequel perfectly matched layer (PML) conditions. In practice, we solve problem (2) in a domain $\widehat{\Omega} = \Omega \cup \Omega_{PML}$, where $\widehat{\Omega} = [0, \ell'_x] \times [0, \ell'_y] \times [0, \ell'_z]$ with $\ell'_w > \ell_w$ for $w = x, y, z$ and $\Omega_{PML} = \widehat{\Omega} \setminus \Omega$. Following [10], we consider the modified wave equation

$$\begin{cases} \dfrac{\partial v}{\partial t}(\underline{x}, t) - tr(\Gamma_1) v(\underline{x}, t) + tr(\Gamma_3) p(\underline{x}, t) - c^2 \Delta p(\underline{x}, t) & \\ \qquad\qquad = \nabla \cdot \underline{\phi}(\underline{x}, t) - \zeta_x \zeta_y \zeta_z \psi(\underline{x}, t), & t \in \mathbb{R}^+, \underline{x} \in \widehat{\Omega}, \\ \dfrac{\partial p}{\partial t}(\underline{x}, t) = v(\underline{x}, t), & t \in \mathbb{R}^+, \underline{x} \in \widehat{\Omega}, \\ \dfrac{\partial \underline{\phi}}{\partial t}(\underline{x}, t) = \Gamma_1 \underline{\phi}(\underline{x}, t) + c^2 \Gamma_2 \nabla p(\underline{x}, t) + c^2 \Gamma_3 \nabla \psi(\underline{x}, t), & t \in \mathbb{R}^+, \underline{x} \in \widehat{\Omega}, \\ \dfrac{\partial \psi}{\partial t}(\underline{x}, t) = p(\underline{x}, t), & t \in \mathbb{R}^+, \underline{x} \in \widehat{\Omega}. \end{cases} \tag{18}$$

where $tr(\cdot)$ is the trace operator, $\underline{\phi}$ and $\psi$ are auxiliary variables, and $\Gamma_1, \Gamma_2$, and $\Gamma_3$ are defined as

$$\Gamma_1 = \begin{bmatrix} -\zeta_x & 0 & 0 \\ 0 & -\zeta_y & 0 \\ 0 & 0 & -\zeta_z \end{bmatrix}, \Gamma_2 = \begin{bmatrix} \zeta_y + \zeta_z - \zeta_x & 0 & 0 \\ 0 & \zeta_x + \zeta_z - \zeta_y & 0 \\ 0 & 0 & \zeta_x + \zeta_y - \zeta_z \end{bmatrix}, \Gamma_3 = \begin{bmatrix} \zeta_y \zeta_z & 0 & 0 \\ 0 & \zeta_x \zeta_z & 0 \\ 0 & 0 & \zeta_x \zeta_y \end{bmatrix}.$$

The functions $\zeta_w(w)$ for $w = \{x, y, z\}$ are positive inside the absorbing layer $\Omega_{PML}$ but vanishes inside $\Omega$. This damping profile can be chosen arbitrarily as a constant, linear, or quadratic function. An example of such profile, for $w = \{x, y, z\}$ is given by

$$\zeta_w(w) = \begin{cases} 0, & 0 \leq w \leq \ell_w, \\ \overline{\zeta}_w \left( \dfrac{w - \ell_w}{\ell'_w - \ell_w} - \dfrac{1}{2\pi} \sin \left( 2\pi \dfrac{w - \ell_w}{\ell'_w - \ell_w} \right) \right), & \ell_w < w < \ell'_w, \\ \overline{\zeta}_w \left( \dfrac{w}{\ell_w - \ell'_w} - \dfrac{1}{2\pi} \sin \left( 2\pi \dfrac{w}{\ell_w - \ell'_w} \right) \right), & \ell_w - \ell'_w < w < 0, \end{cases}$$

where $\overline{\zeta}_w$ is a constant related to the relative reflection $R = \dfrac{c}{(\ell'_w - \ell_w)} \log \left( \dfrac{1}{R} \right)$, a measure of the amount of reflection that occurs when a wave encounters an interface. To approximate (18) we proceed as follows. For any $(i, j, k) \in D_x \times D_y \times D_z$ and any $n \in \mathbb{N}$ we define

$$\varphi^{\widehat{n}}_{i,j,k} = \frac{\varphi^{n+\frac{1}{2}}_{i,j,k} + \varphi^{n-\frac{1}{2}}_{i,j,k}}{2}, \quad \text{with} \quad \varphi^{n+\frac{1}{2}}_{i,j,k} = \frac{\varphi^{n+1}_{i,j,k} + \varphi^{n}_{i,j,k}}{2},$$

for $\varphi = \{\psi, p\}$, and set

$$(\nabla \cdot \underline{\phi})^n_{i,j,k} = \frac{1}{dh} \left( \sum_{h=-2}^{2} b_h \phi^n_{i+h,j,k} + \sum_{h=-2}^{2} b_h \phi^n_{i,j+h,k} + \sum_{h=-2}^{2} b_h p^n_{i,j,k+h} \right)$$

with $b_{-2} = 1/12, b_{-1} = -2/3, b_0 = 0, b_1 = 2/3, b_2 = -1/12$. System (18) is discretized by means of the following scheme:

$$\begin{aligned} v_{i,j,k}^{n+1} = {} & \frac{\left(1 - \frac{dt}{2}(\zeta_{x;i} + \zeta_{y;j} + \zeta_{z;k})\right) v_{i,j,k}^{n} + dtc^2(\Delta p)_{i,j,k}^{n}}{1 + \frac{dt}{2}(\zeta_{x;i} + \zeta_{y;j} + \zeta_{z;k})} \\ & - dt \frac{(\zeta_{y;j}\zeta_{z;k} + \zeta_{x;i}\zeta_{z;k} + \zeta_{x;i}\zeta_{y;j})p_{i,j,k}^{n} - (\nabla \cdot \underline{\phi})_{i,j,k}^{n} + (\zeta_{x;i}\zeta_{y;j}\zeta_{z;k})\psi_{i,j,k}^{\widehat{n}}}{1 + \frac{dt}{2}(\zeta_{x;i} + \zeta_{y;j} + \zeta_{z;k})}, \end{aligned}$$

for the first equation and

$$\begin{aligned} p_{i,j,k}^{n+1} &= p_{i,j,k}^{n} + dtv_{i,j,k}^{n+1}, \\ \phi_{i,j,k}^{n+1} &= \frac{\left(1 - \frac{dt}{2}\zeta_{x;i}\right) \phi_{i,j,k}^{n} + dt(\zeta_{y;j} + \zeta_{z;k} - \zeta_{x;i}) \dfrac{p_{i,j,k}^{n+\frac{1}{2}} - p_{i,j,k}^{n+\frac{1}{2}}}{dh} + dt(\zeta_{y;j}\zeta_{z;k}) \dfrac{\psi_{i,j,k}^{n+\frac{1}{2}} - \psi_{i,j,k}^{n+\frac{1}{2}}}{dh}}{1 + \frac{dt}{2}\zeta_{x;i}}, \\ \psi_{i,j,k}^{n+\frac{1}{2}} &= \psi_{i,j,k}^{n-\frac{1}{2}} + dtp_{i,j,k}^{n}, \end{aligned}$$

for the remaining ones.

# MOX Technical Reports, last issues

Dipartimento di Matematica
Politecnico di Milano, Via Bonardi 9 - 20133 Milano (Italy)

**47/2024** Franco, N.R.; Brugiapaglia, S.
*A practical existence theorem for reduced order models based on convolutional autoencoders*

**44/2024** Fumagalli, I.
*Discontinuous Galerkin method for a three-dimensional coupled fluid-poroelastic model with applications to brain fluid mechanics*

**45/2024** Fumagalli, A.; Patacchini, F. S.
*Numerical validation of an adaptive model for the determination of nonlinear-flow regions in highly heterogeneos porous media*

**46/2024** Riccobelli, D.; Ciarletta, P.; Vitale, G.; Maurini, C.; Truskinovsky, L.
*Elastic Instability behind Brittle Fracture*

**43/2024** Antonietti, P.F.; Corti, M., Martinelli, G.
*Polytopal mesh agglomeration via geometrical deep learning for three-dimensional heterogeneous domains*

**42/2024** Fois, M.; Katili M. A.; de Falco C.; Larese A.; Formaggia L.
*Landslide run-out simulations with depth-averaged models and integration with 3D impact analysis using the Material Point Method*

**41/2024** Bergonzoli, G.; Rossi, L.; Masci, C.
*Ordinal Mixed-Effects Random Forest*

**40/2024** Carrara, D.; Regazzoni, F.; Pagani, S.
*Implicit neural field reconstruction on complex shapes from scattered and noisy data*

**39/2024** Bartsch, J.; Buchwald, S.; Ciaramella, G.; Volkwein, S.
*Reconstruction of unknown nonlienar operators in semilinear elliptic models using optimal inputs*

**38/2024** Tonini, A., Regazzoni, F., Salvador, M., Dede', L., Scrofani, R., Fusini, L., Cogliati, C., Pontone, G., Vergara, C., Quarteroni, A.
*Two new calibration techniques of lumped-parameter mathematical models for the cardiovascular system*